



Magnetic Energy Release, Plasma Dynamics, and Particle Acceleration in Relativistic Turbulent Magnetic Reconnection

Fan Guo¹ , Xiaocan Li² , William Daughton¹ , Hui Li¹ , Patrick Kilian^{1,3} , Yi-Hsin Liu² , Qile Zhang¹ , and Haocheng Zhang^{4,5}

¹Los Alamos National Laboratory, NM 87545, USA

²Dartmouth College, Hanover, NH 03750, USA

³Space Science Institute, Boulder, CO 80301, USA

⁴New Mexico Consortium, Los Alamos, NM 87544, USA

⁵Department of Physics and Astronomy, Purdue University, West Lafayette, IN 47907, USA

Received 2020 August 6; revised 2021 May 16; accepted 2021 June 2; published 2021 September 29

Abstract

In strongly magnetized astrophysical plasma systems, magnetic reconnection is believed to be the primary process during which explosive energy release and particle acceleration occur, leading to significant high-energy emission. Past years have witnessed active development of kinetic modeling of relativistic magnetic reconnection, supporting this magnetically dominated scenario. A much less explored issue in studies of relativistic reconnection is the consequence of three-dimensional dynamics, where turbulent structures are naturally generated as various types of instabilities develop. This paper presents a series of three-dimensional, fully kinetic simulations of relativistic turbulent magnetic reconnection (RTMR) in positron–electron plasmas with system domains much larger than kinetic scales. Our simulations start from a force-free current sheet with several different modes of long-wavelength magnetic field perturbations, which drive additional turbulence in the reconnection region. Because of this, the current layer breaks up and the reconnection region quickly evolves into a turbulent layer filled with coherent structures such as flux ropes and current sheets. We find that plasma dynamics in RTMR is vastly different from its 2D counterpart in many aspects. The flux ropes evolve rapidly after their generation, and can be completely disrupted by the secondary kink instability. This turbulent evolution leads to superdiffusive behavior of magnetic field lines as seen in MHD studies of turbulent reconnection. Meanwhile, nonthermal particle acceleration and the timescale for energy release can be very fast and do not depend strongly on the turbulence amplitude. The main acceleration mechanism is a Fermi-like acceleration process supported by the motional electric field, whereas the nonideal electric field acceleration plays a subdominant role. We also discuss possible observational implications of three-dimensional RTMR in high-energy astrophysics.

Unified Astronomy Thesaurus concepts: [High energy astrophysics \(739\)](#)

Supporting material: animations

1. Introduction

Magnetic reconnection is one of the fundamental plasma processes in the universe, where free magnetic energy stored in the antiparallel magnetic field component of current sheets can release rapidly and be converted into energy contained in plasma bulk flow, and thermal and nonthermal distributions (Biskamp 2000; Priest & Forbes 2007). In strongly magnetized astrophysical systems, magnetic reconnection is an efficient mechanism for converting magnetic energy into particle heating and acceleration, and subsequent high-energy emissions. Relativistic magnetic reconnection in the magnetically dominated regime (magnetization parameter $\sigma = B^2/(8\pi w) \gg 1$, where w is the enthalpy density) is often invoked to explain high-energy particles and emissions from objects such as pulsar wind nebulae (Coroniti 1990; Lyubarsky & Kirk 2001; Kirk & Skjæraasen 2003; Arons 2012; Hoshino & Lyubarsky 2012), jets from active galactic nuclei (de Gouveia dal Pino & Lazarian 2005; Giannios et al. 2009; Yan & Zhang 2015; Zhang et al. 2015, 2017, 2018; Nathanael et al. 2020; Zhang & Giannios 2021), and gamma-ray bursts (Zhang & Yan 2011; McKinney & Uzdensky 2012).

Past years have seen active development in theoretical modeling of relativistic magnetic reconnection, supporting the magnetically dominated scenario (Blackman & Field 1994;

Lyutikov 2003; Lyubarsky 2005; Comisso & Asenjo 2014; Liu et al. 2017, 2020). Recently, a large range of two-dimensional (2D), fully kinetic studies have explored reconnection in the magnetically dominated regime in detail, particularly on the reconnection properties (Liu et al. 2015, 2017, 2020), particle acceleration (Sironi & Spitkovsky 2014; Guo et al. 2014, 2015, 2016, 2019; Werner et al. 2016), and possible radiation signatures (Sironi et al. 2016; Petropoulou et al. 2016; Zhang et al. 2018, 2020). In the magnetically dominated regime, reconnection in a thin current sheet proceeds at a rate with inflow speed $v_{\text{in}} \sim 0.1$ times the upstream Alfvén speed V_A close to the maximum local rate (Liu et al. 2017, 2020). While the maximum outflow Lorentz factor can approach $\Gamma_{\text{out}} \sim \sqrt{\sigma + 1}$, it can be significantly limited by a guide field B_g so $\Gamma_{\text{out}} \sim \sqrt{(\sigma + 1)/(\sigma_g + 1)}$, where $\sigma_g = B_g^2/(8\pi w)$ (Liu et al. 2015). Relativistic reconnection seems to be a source of efficient nonthermal particle acceleration (Sironi & Spitkovsky 2014; Guo et al. 2014, 2015; Werner et al. 2016). In 2D simulations, it was found, through several different analyses, that a Fermi-like acceleration driven by plasmoid motion dominates the acceleration process (Guo et al. 2014, 2015, 2019)⁶ and leads to formation of power-law

⁶ See Drake et al. (2006), Dahlin et al. (2014, 2017), and Li et al. (2017, 2018a, 2019a, 2019b) for a nonrelativistic description.

energy distributions $f \propto \varepsilon^{-p}$ in the weak-guide-field regime. In particle-in-cell (PIC) simulations of weak-guide-field relativistic reconnection, the plasma dynamics and particle acceleration in 2D relativistic reconnection are controlled by plasmoids as current sheets continuously generate and break up into interacting plasmoids (Daughton & Karimabadi 2007; Guo et al. 2015; Sironi et al. 2016; Liu et al. 2020). See Guo et al. (2020) for a review of the primary acceleration mechanism, power-law formation, and reconnection physics.

While 2D simulations of antiparallel relativistic reconnection have been carried out extensively, there have been only limited studies on 3D magnetically dominated reconnection with $\sigma \gg 1$ (Sironi & Spitkovsky 2014; Guo et al. 2014, 2015; Werner & Uzdensky 2017). It was verified that 3D physics does not strongly influence the development of a nonthermal power-law energy spectrum,⁷ but the acceleration mechanism has not been studied as carefully as in 2D simulations. In addition, the timescale for energy release represented by the reconnection rate (Guo et al. 2015) does not change strongly in 3D.⁸ However, there has been a lack of exploration of 3D plasma dynamics and its possible observational implications. It is known now that a range of secondary instabilities can grow and lead to turbulence in the reconnection layer (Bowers & Li 2007; Zenitani & Hoshino 2008; Daughton et al. 2011; Guo et al. 2015; Kowal et al. 2020). Therefore, turbulent magnetic reconnection is a more likely picture for the realistic situation and conclusions based on 2D reconnection need to be examined carefully using 3D simulations.

To summarize what we have discussed so far: a major uncertainty of relativistic reconnection studies is the role of three-dimensional dynamics and turbulence. Earlier turbulent reconnection studies using various numerical approaches have found that pre-existing turbulence and self-generated turbulence can both exist, but their roles in magnetic energy dissipation, plasma dynamics, and particle acceleration remain controversial (Bowers & Li 2007; Huang & Bhattacharjee 2016; Beresnyak 2017; Kowal et al. 2017; Lazarian & Vishniac 1999; Matthaeus & Lamkin 1985, 1986; Loureiro et al. 2009; Daughton et al. 2011, 2014; Yang et al. 2020; Leake et al. 2020). This highlighted study is designed to explore some of the aspects when magnetic reconnection occurs in a turbulent state, with focus on the relativistic regime, which we now refer to as relativistic turbulent magnetic reconnection (RTMR).

In this paper, a number of large-scale (system size \gg kinetic scale), three-dimensional, fully kinetic simulations are carried out using the Los Alamos VPIC code.⁹ This is made possible on the Trinity machine during its open science period. We focus on simulations with a positron–electron pair plasma that minimize the kinetic range and maximize the ratio between system size and kinetic scale ($L/d_e \sim 10^3$). Different from typical kinetic studies, we have added a new set of initial perturbations to drive extra turbulence in the simulation domain. Because of this, the reconnection layer quickly develops into a turbulent state. The flux ropes, different from their corresponding 2D magnetic islands, evolve dynamically after their generation, and can be completely disrupted by the secondary kink instability. We find that while the reconnection X-points are strongly perturbed by the injected

and self-generated fluctuation due to secondary tearing and kink instabilities, acceleration of high-energy particles is robust and leads to the formation of a power-law distribution. In addition, the normalized reconnection rate is of the order of $R \sim 0.1$. We show that for the case of antiparallel reconnection the Fermi-like acceleration mechanism is the dominant process. During the reconnection process, thin reconnection layers develop continuously and the peak reconnection rate is nearly independent of the injected magnetic energy, suggesting the reconnection physics is primarily controlled by kinetic-scale physics in our kinetic simulations. The rest of the paper is organized as follows: Section 2 describes numerical methods, setups, and important parameters. Section 3 discusses the primary simulation results. We discuss observational implications in Section 4, and conclusions are drawn in Section 5.

2. Numerical Simulations

The 3D simulations presented here start from a force-free current layer with $\mathbf{B} = B_0 \tanh(z/\lambda) \hat{x} + B_0 \sqrt{\text{sech}^2(z/\lambda) + b_g^2} \hat{y}$, where B_0 is the strength of the reconnecting magnetic field, b_g is the strength of the guide field B_g normalized by B_0 , and λ is the half-thickness of the current sheet (Guo et al. 2014, 2015, 2019; Li et al. 2017, 2018a, 2019b). The plasma consists of electron–positron pairs (mass ratio $m_p/m_e = 1$). The initial distributions are Maxwellian with a uniform density n_0 and temperature ($T_p = T_e$). For the simulations discussed in this paper, the amount of thermal energy per particle is $\sim m_e c^2$. Particles in the sheet have a drift velocity $\mathbf{u}_p = -\mathbf{u}_e$, and that gives rise to a current density satisfying Ampère’s law $\nabla \times \mathbf{B} = 4\pi \mathbf{J}$. The simulations are performed using the VPIC code (Bowers et al. 2008), which solves the relativistic Vlasov–Maxwell equation system. We have performed simulations with $\sigma_e = B_0^2 / (4\pi n_e m_e c^2) = 6$ –1600. We mainly focus on the case with $\sigma_e = 100$, corresponding to $\omega_{pe}/\Omega_{ce} = 0.1$, where $\omega_{pe} = \sqrt{4\pi n_e e^2/m_e}$ is the plasma frequency and $\Omega_{ce} = eB_0/(m_e c)$ is the electron gyrofrequency (without relativistic corrections). In the simulations the half-thickness is set to be $\lambda = 6d_e$ for simulations with $\sigma_e < 100$, $\lambda = 12d_e$ for $\sigma_e = 400$, and $\lambda = 24d_e$ for $\sigma_e = 1600$ to ensure drift speed $u_i < c$. The presented electric and magnetic fields are normalized by B_0 . The current density is normalized by $J_0 = en_0 c$. The domain size is $L_x \times L_z \times L_y = 1000d_e \times 500d_e \times 500d_e$, where $d_e = c/\omega_{pe}$ is the inertial length. The resolution of the simulations is $N_x \times N_z \times N_y = 4096 \times 2048 \times 2048$ or 17.2 billion cells. All simulations used 300 particles (both species together) per cell with the total number of particles being ~ 5.2 trillion. A list of simulation runs and their parameters can be found in Table 1. Simulations employed periodic boundary conditions in the x - and y -directions, and in the z -direction used conducting boundaries for the fields and reflecting boundaries for the particles. A long-wavelength perturbation is included to create a dominating X-line at the center of the simulation domain. Different from the earlier simulations, we also inject an array of perturbations with different wavelengths at $t = 0$:

$$\delta \mathbf{B}/B_0 = \sum_{j,k} a_0 \cos(k_{jx} + k_{kz} + \phi_{j,k}) \hat{y} + \sum_{l,n} a_0 \cos(k_{lx} + k_{ny} + \phi_{l,n}) \hat{z} \quad (1)$$

⁷ However, see Li et al. (2019b) and Zhang et al. (2021) for the effect of 3D physics on nonthermal particle acceleration in nonrelativistic reconnection.

⁸ See also nonrelativistic studies (Liu et al. 2013; Daughton et al. 2014).

⁹ <https://github.com/lanl/vpic>

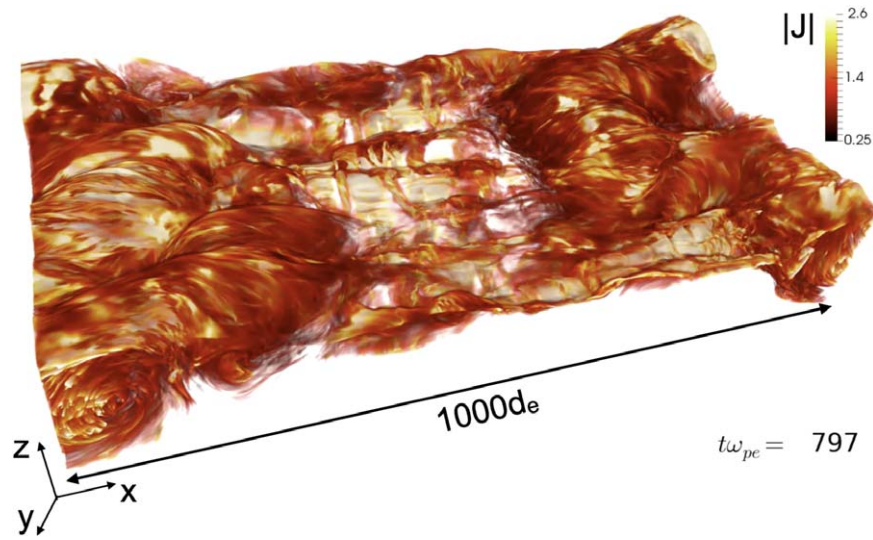


Figure 1. The distribution (volume rendering) of the magnitude of the current density in the reconnection region at $\omega_{pe}t = 797$ for the standard run 3D-1. Under the influence of injected turbulence, the current sheet breaks into a turbulent reconnection region filled with many structures such as flux ropes and current sheets.

Table 1
List of Simulation Runs and their Parameters

Run	σ_e	System size	b_g	$\delta B^2/B_0^2$
3D-1 [S]	100	$1000d_e \times 500d_e \times 500d_e$	0	0.1
3D-2	400	$1000d_e \times 500d_e \times 500d_e$	0	0.1
3D-3	1600	$1000d_e \times 500d_e \times 500d_e$	0	0.1
3D-4	25	$1000d_e \times 500d_e \times 500d_e$	0	0.1
3D-5	6	$1000d_e \times 500d_e \times 500d_e$	0	0.1
3D-6	100	$1000d_e \times 500d_e \times 500d_e$	1	0.1
3D-7	100	$1000d_e \times 500d_e \times 500d_e$	0	0.0
3D-8	100	$1000d_e \times 500d_e \times 500d_e$	0	0.2
3D-9	100	$1000d_e \times 500d_e \times 500d_e$	0	0.4
3D-10	100	$1000d_e \times 500d_e \times 500d_e$	0	0.1

with the summed wave power $(\delta B/B_0)^2$ up to 0.4 to initiate background turbulence at the beginning of the simulation. These initially injected perturbations have 10 modes with wavelengths longer than the initial thickness of the current sheet. The simulation lasts $\omega_{pe}t \approx 1100$, which is about the time for a light wave to travel through $\tau_c = L_x/c$. The timescale to traverse the thickness of the current sheet, however, is much shorter. In addition to the antiparallel case ($b_g = 0$), we also included a case with $b_g = 1$ to examine the influence of a guide field.

In VPIC simulations, we have implemented a particle tracing module to output particle trajectories and find the electric field, magnetic field, and bulk fluid velocity at particle locations (Guo et al. 2016, 2019; Li et al. 2018a, 2019b; Kilian et al. 2020), and therefore we can evaluate the relative importance of the motional electric field $\mathbf{E}_m = -\mathbf{V} \times \mathbf{B}/c$ and nonideal electric field $\mathbf{E}_n = \mathbf{E} + \mathbf{V} \times \mathbf{B}/c$ based on the generalized Ohm's law (Guo et al. 2019). In this study, we uniformly select one of every 50,000 particles (~ 100 million in total) at the beginning of the simulation and analyze their acceleration to high energy. This allows us to quantitatively determine the contribution of Fermi-like acceleration and nonideal electric field in 3D simulations, respectively.

3. Simulation Results

3.1. Plasma Dynamics

3.1.1. General Overview of RTMR

The imposed wave perturbation leads to the evolution of current sheets in a fully 3D fashion. The initial current sheet quickly breaks into a broad reconnection region filled with nonlinear structures such as flux ropes and current sheets, evolving into an RTMR state. Figure 1 shows a volume-rendering diagram of the magnitude of the current density with $\sigma_e = 100$ at $\omega_{pe}t = 797$ (standard run 3D-1). As reconnection proceeds, antiparallel magnetic field from upstream continuously feeds into the reconnection region, forming new current sheets in different local regions, and the new current sheets further break into small-scale flux ropes (see below for more discussion on flux rope dynamics). This process happens over and over again in a cyclic way.

Figure 2 provides four additional snapshots to show the time evolution of the reconnection layer (see also the animation in the online Journal and on YouTube¹⁰). While their 2D counterparts are well studied (Daughton et al. 2006; Daughton & Karimabadi 2007; Liu et al. 2015, 2020), the 3D simulations reveal a picture far more complicated and rich in structures. To see those fine structures more closely, one can review Figure 3 for four 2D cuts at different time steps as well as an animated version in the online Journal and on YouTube.¹¹ For the simulations we present here, the kinetic layers $\sim d_e$ are still continuously generated, and this feature is sustained throughout the dynamical development of reconnection, indicating that kinetic effects may still be important for breaking reconnecting field lines even when the system is turbulent and the largest dimension L_x is about a thousand times larger than the kinetic scale. Importantly, such a single d_e -scale diffusion region often dominates the primary X-line that separates the reversal outflow jets. For kinetic simulations we have carried out so far, it appears that the current sheet always collapses to a thin sheet with thickness comparable to kinetic scale in the weak

¹⁰ <https://youtu.be/-2EsinquZjA>.

¹¹ <https://youtu.be/5-eL9oXXCLS>

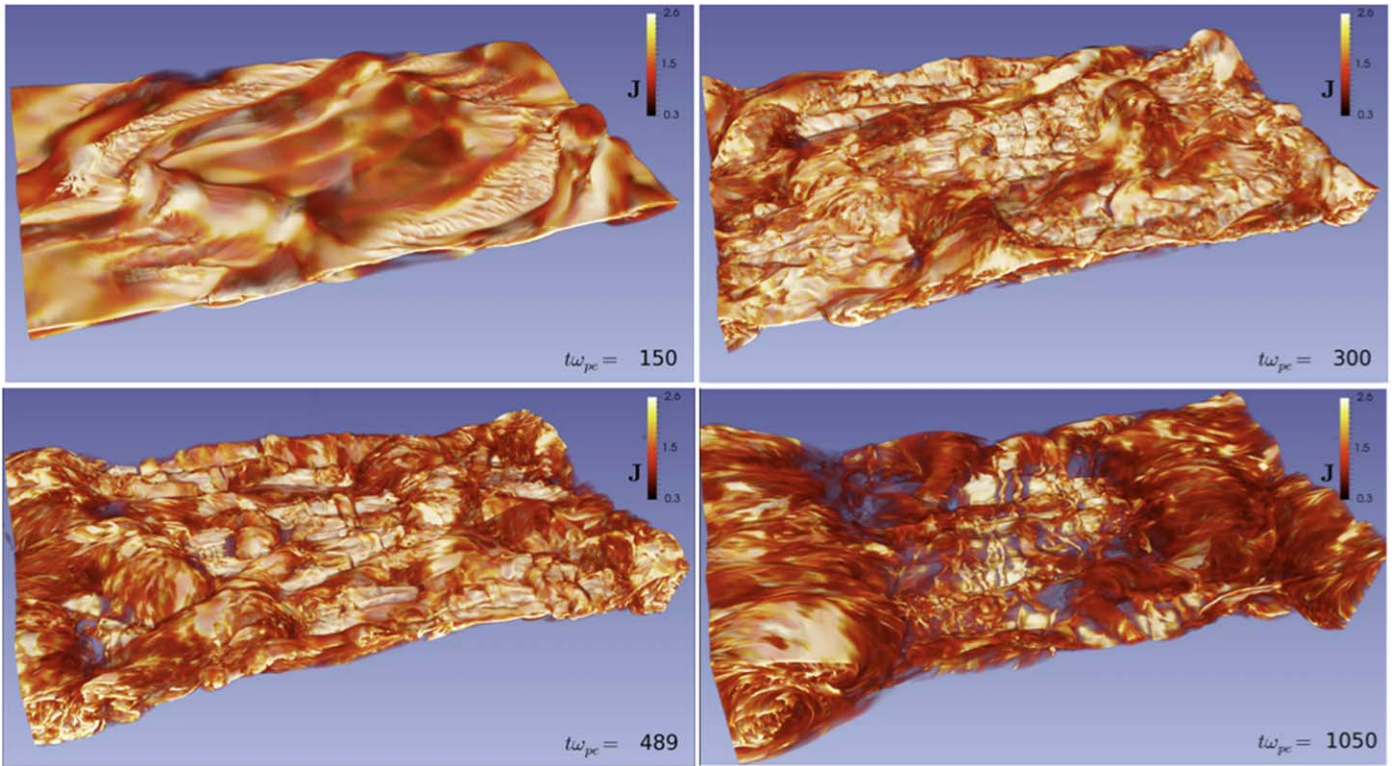


Figure 2. Four snapshots of current density showing the time evolution of the reconnection layer for the run 3D-1. An animation of the time evolution is available in the online Journal. Upstream magnetic field continuously feeds into the reconnection region, forming new current sheets, and the current sheets keeps breaking into flux ropes. The animated version proceeds from $\omega_{pe}t = 0-1050$.

(An animation of this figure is available.)

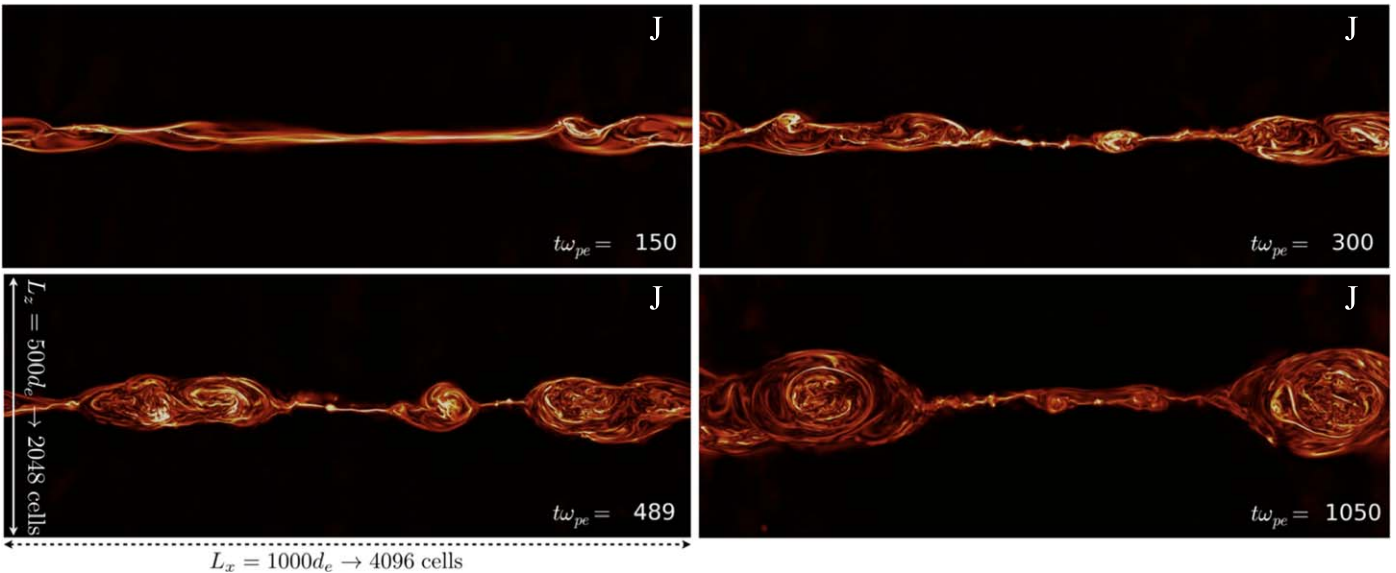


Figure 3. 2D cuts of current density at four different time steps for the run 3D-1. An animation of the current density is available in the online Journal. Kinetic structures with thickness $\sim d_e$ are continuously generated even for the large-scale turbulent reconnection system. The animated version proceeds from $\omega_{pe}t = 0-1050$.

(An animation of this figure is available.)

guide field limit. The cyclic generation of plasmoids is likely related to the loss of current sheet equilibrium due to the depleted pressure caused by reconnection (Liu et al. 2020).

To reveal the turbulent nature of the reconnection layer, we plot the magnetic and kinetic power spectra at different simulation times in Figure 4. The embedded figures are the evolution of magnetic field energy with “ \times ” signs indicating

times when those power spectra are measured. The magnetic power spectrum above kinetic scale $kd_e < 1$ resembles a power-law “inertial” range with slope about ~ -2.7 , decaying in general as magnetic field energy is converted into particle energy. Meanwhile, the kinetic energy spectra are more or less in consistency with the classic $-5/3$ spectrum. More detailed analysis (not shown) suggests that the magnetic power and

kinetic power with wavenumber vector in the reconnection plane (x - z) are much stronger than along the current sheet direction (the y -direction). The slope of the magnetic power spectra appears to be strongly mediated by reconnection, likely due to different processes such as forward cascade and inverse cascade through secondary instabilities and flux rope merging (Bowers & Li 2007; Daughton et al. 2014; Guo et al. 2015; Huang & Bhattacharjee 2016; Loureiro & Boldyrev 2018; Yang et al. 2020; Zhou et al. 2020; Kowal et al. 2020). However, we acknowledge that this issue is still under debate. For example, Huang & Bhattacharjee (2016) present resistive MHD simulations with high Lundquist number, showing that several properties of reconnection-driven turbulence, such as the magnetic energy spectrum and anisotropy, clearly deviated from the classical Goldreich–Sridhar model. However, Kowal et al. (2017) presented simulations over a much longer timescale, and they showed that the slope gradually evolves toward $5/3$. Due to the diagnostics added on for particle acceleration, our simulations only extend to a limit time. We defer more studies targeting this issue to a future publication.¹² We further look into the structure functions and the scale-generated turbulent eddy anisotropy in the reconnection-generated turbulence in Figure 5. The contours of the structure functions shown in Figures 5(a) and (c) clearly show elongated turbulent eddies along the local magnetic field direction. The turbulence anisotropy scaling (Figures 5(b) and (d)) shows that the turbulence is scale-independent at small scales ($l_{\parallel} < 20d_e$) and then resembles Goldreich–Sridhar (GS) scaling $l_{\parallel} \sim l_{\perp}^{2/3}$ (Goldreich & Sridhar 1995, 1997) at larger scales, similar to the MHD simulation results of Kowal et al. (2017).

3.1.2. Dynamical Evolution of Flux Ropes

During RTMR, numerous new, small-scale flux ropes keep emerging from newly formed current layers. Figure 6 (see also the animation in the online Journal and on YouTube¹³) shows a part of the simulation domain ($250 < x/d_e < 680$ and $250 < y/d_e < 500$) in the reconnection layer where multiple flux ropes are generated from the layer. This process is sustained throughout the simulation. Each of the flux ropes appears very different from cylindrical magnetic structures indicated by 2D simulations (Guo et al. 2015; Sironi et al. 2016). In three dimensions, the flux ropes can be very dynamical and are unstable to the kink instability. Next, we focus on a flux rope indicated by the white box in Figure 6. Figure 7 and the online animation¹⁴ provide a zoom-in view for the evolution of this flux rope. At $\omega_{pe}t = 621.7$, the flux rope (indicated by the arrow) just emerges from the reconnection layer and has a quasi-2D structure. However, it soon starts to twist because of the nonlinear development of the kink instability and possibly additional velocity shear. The whole flux rope breaks as it is strongly distorted, and is eventually dissolved in the reconnection layer. We find that individual flux ropes do interact and merge with each other, evolving into larger flux ropes, but

¹² Note that the often used periodic boundary conditions may not be appropriate for studying the long-term evolution of the system beyond several light-crossing times τ_c . Our 3D simulations with reduced domain sizes (not shown) suggest that when the simulations extend to $\sim 10\tau_c$, the reconnection process becomes stagnated with no net outflow or inflow, while some local patches of reconnection still occur in the 3D simulations and consume the upstream magnetic field.

¹³ <https://youtu.be/FWI-Fhvgsrc>

¹⁴ <https://youtu.be/WXd1kF5wozM>

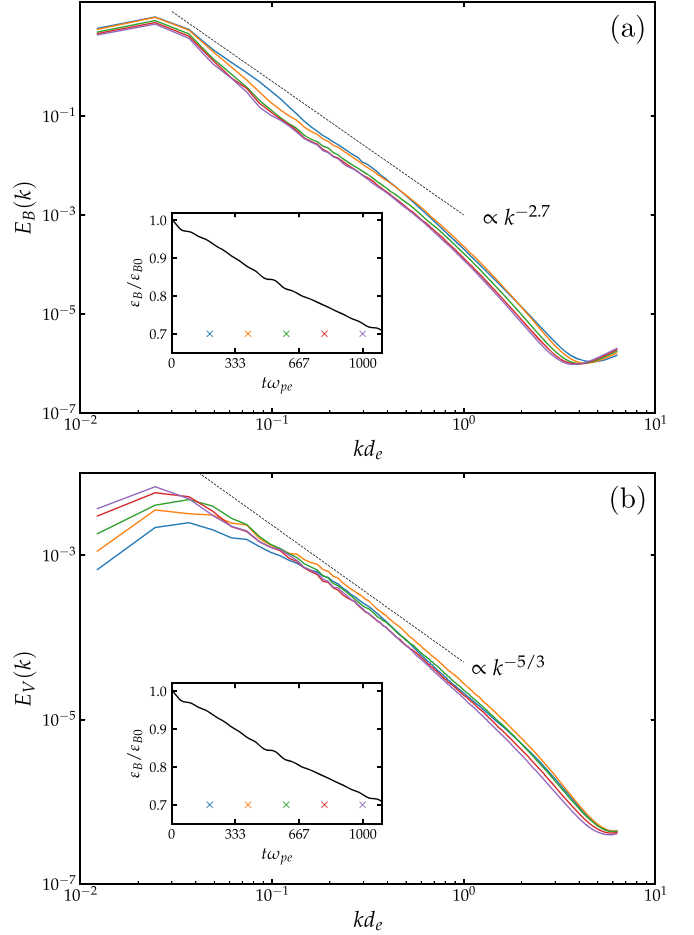


Figure 4. Magnetic (a) and kinetic (b) power spectra as a function of wavenumber at different times in the standard run 3D-1 indicated by “x” signs in the insets. The insets also show the evolution of magnetic energy in the system. The magnetic power spectra with scales above the kinetic scale resemble a power law with a slope about -2.7 , whereas the kinetic energy spectra agree roughly with a $-5/3$ slope.

details are much more complicated than for their 2D counterparts (e.g., Guo et al. 2015; Sironi et al. 2016; Zhang et al. 2018). While recent studies have explored the consequence of radiation signatures of 2D relativistic plasmoid reconnection (Petropoulou et al. 2016; Zhang et al. 2018), we show here that when the simulations extend to 3D, the reconnection layer becomes very turbulent and plasma dynamics—especially the behavior of the flux ropes—is significantly different from the corresponding structures (plasmoids) in 2D simulations. Exploring 3D effects in those simulations is important to confirm the robustness of previous 2D results.

3.1.3. Outflow structures

It is instructive to explore the reconnection outflow and its structures in the turbulent reconnection layer and how laminar reconnection is modified by turbulence. Figure 8 shows the outflow speed $\langle V_x \rangle$ averaged over the y -direction at several different snapshots. We find that the averaged outflow speed is significantly slower than the theoretical value $V_{\text{out}} = \sqrt{\sigma/(1 + \sigma)}c$ and earlier reported 2D results (Guo et al. 2015; Sironi et al. 2016). Instead, the averaged speed in the reconnection layer can only reach $\sim 0.4c$. The whole reconnection layer appears to be broadened although kinetic layers still

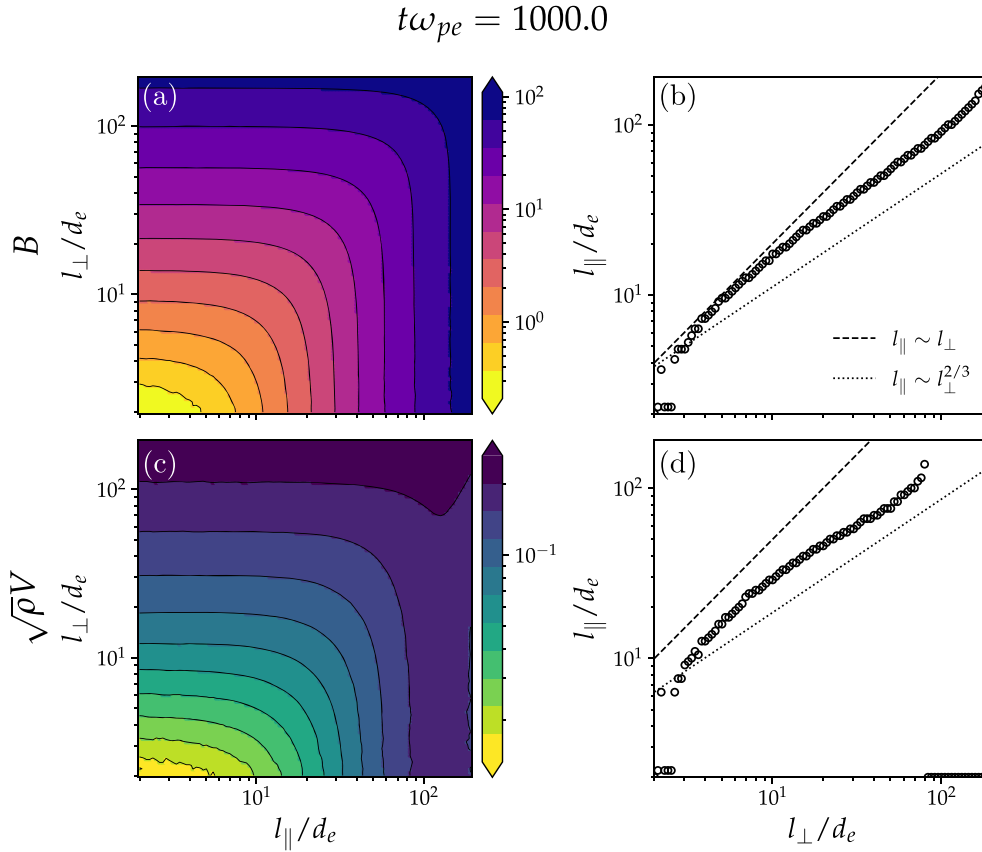


Figure 5. Second-order structure functions of the magnetic field and kinetic flow $\mathbf{w} = \sqrt{\rho}\mathbf{V}$ in the standard run 3D-1 (panels (a) and (c)), following the method of Cho & Vishniac (2000). In the method, the local magnetic fields are calculated as $\mathbf{B}_l = (\mathbf{B}(\mathbf{r}_1) + \mathbf{B}(\mathbf{r}_2))/2$, and the second-order structure functions for \mathbf{B} and \mathbf{w} are $F_2^b(l_{\parallel}, l_{\perp}) = \langle |\mathbf{B}(\mathbf{r}_1) - \mathbf{B}(\mathbf{r}_2)|^2 \rangle$ and $F_2^w(l_{\parallel}, l_{\perp}) = \langle |\mathbf{w}(\mathbf{r}_1) - \mathbf{w}(\mathbf{r}_2)|^2 \rangle$, respectively. $l_{\parallel} = \mathbf{l} \cdot \mathbf{B}_l / |\mathbf{B}_l|$ and $l_{\perp} = \sqrt{l^2 - l_{\parallel}^2}$, where $\mathbf{l} = \mathbf{r}_2 - \mathbf{r}_1$ and $l = |\mathbf{l}|$. Panels (b) and (d) represent the relationships between parallel scale l_{\parallel} and perpendicular scale l_{\perp} of the contours in panels (a) and (c), measuring the scale dependence of turbulent eddy anisotropy. The dashed and dotted lines represent the relations $l_{\parallel} \sim l_{\perp}$ (scale-independent) and $l_{\parallel} \sim l_{\perp}^{2/3}$ (GS theory), respectively.

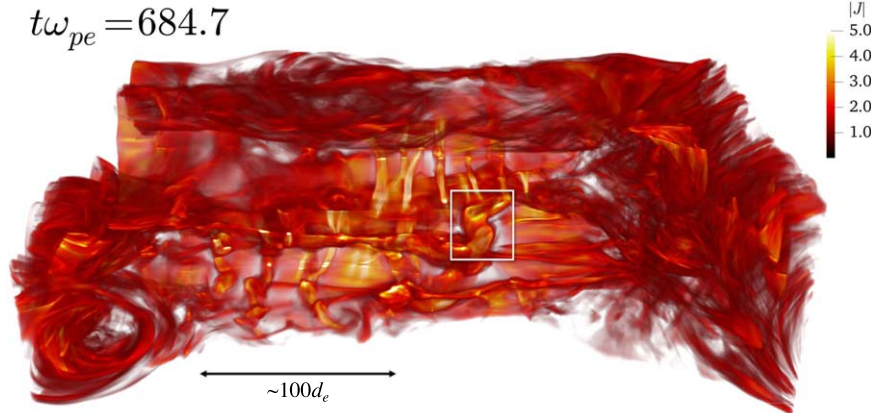


Figure 6. Volume rendering of magnitude of current density for a selected region ($250 < x/d_e < 680$ and $250 < y/d_e < 500$) in the reconnection layer where multiple flux ropes are generated during magnetic reconnection. An animation of the generation of the flux ropes is available in the online Journal. A flux rope is indicated using a white box for further study in Figure 7. The animation proceeds from $\omega_{pe}t = 550.9$ – 1046.7 .

(An animation of this figure is available.)

develop locally (Figure 3). A similar analysis that used resistive MHD simulations has seen similar effects (Huang & Bhattacharjee 2016; Kowal et al. 2017). Figure 9 shows three different x - z cuts at different y -positions at time $\omega_{pe}t = 797$. The primary X-lines at different y -positions that emit reversal jets appear to be much thinner (close to the kinetic scale). However,

the main X-line location in the reconnection plane varies in the y -direction, leading to a slower outflow when averaged over a finite distance. This is because the nonlinear development of the kink mode disturbs X-lines and the X-point region so they cannot align along the y -direction as in 2D. When averaged out in 3D, the island structure is no longer significant.

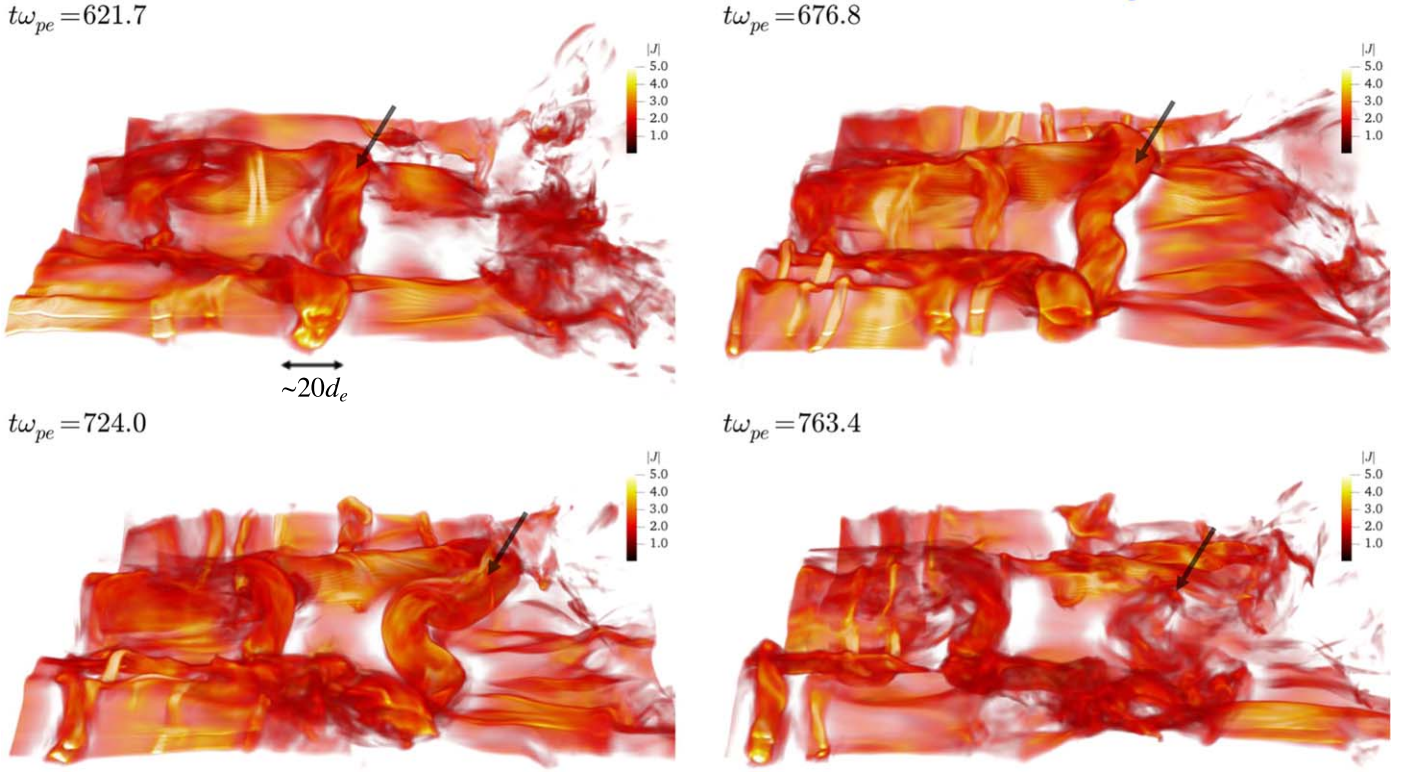


Figure 7. Several snapshots of current density showing the evolution of a flux rope indicated in Figure 6. An animation of this flux rope is available in the online Journal. The flux rope is disrupted quickly after it emerges during the simulation. The animation proceeds from from $\omega_{pe}t = 550.9$ – 787.0 . (An animation of this figure is available.)

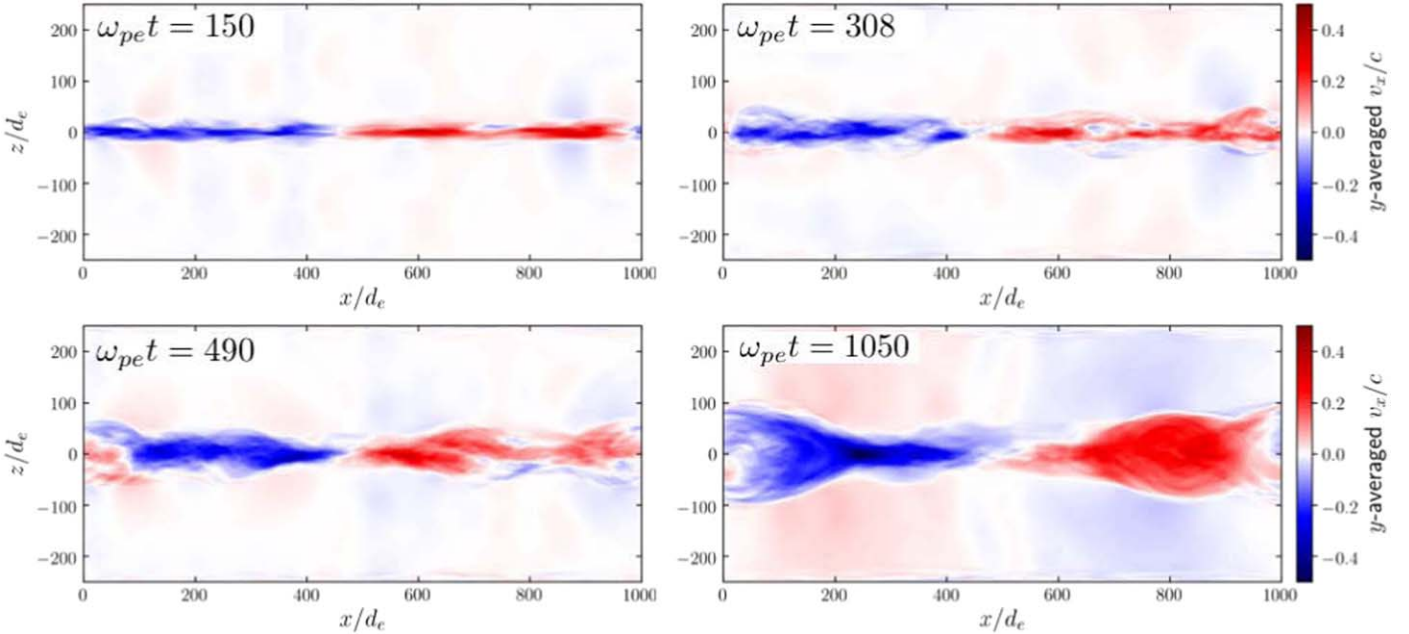


Figure 8. The flow velocity V_x averaged over the y -direction. In relativistic turbulent reconnection, the averaged outflow speed is significantly reduced from the theoretical limit $V_A = \sqrt{\sigma/(\sigma + 1)}c$ to a fraction of the light speed.

3.2. Particle Acceleration and Its Mechanism

3.2.1. Energy Spectrum

Figure 10 shows the time evolution of particle energy spectra integrated over the whole simulation for $\sigma_e = 100$ (run 3D-1). The resulting energy spectrum eventually resembles a power-law

distribution $f \propto (\gamma - 1)^{-p}$ with $p \sim 1.8$. This is similar—but somewhat softer than—earlier results from 2D and 3D simulations starting from a laminar layer (Guo et al. 2014, 2015). Figure 11 shows the energy spectra for a number of 3D runs from $\sigma_e = 6$ to 1600 with $\delta B^2/B_0^2 = 0.1$. We observe clear signatures of nonthermal power-law distributions when $\sigma_e > 1$.

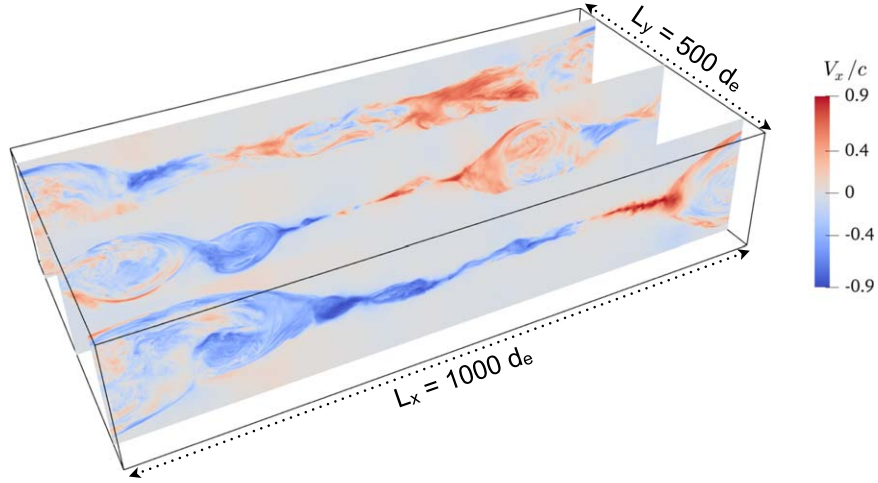


Figure 9. Three 2D cuts for the outflow speed V_x at different y -locations. Because of nonlinear development of instabilities and turbulence, the primary “X-lines” in the 2D planes are located differently in x -position along the y axis.

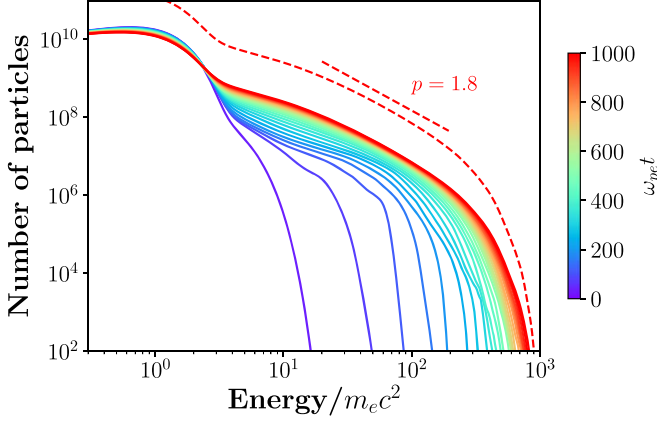


Figure 10. Particle energy spectrum at different simulation times for the standard run. The spectrum at the last time step is replotted and shifted up by a factor of 10. The spectral index is $p = 1.8$.

The spectral index changes from $p = 4$ for $\sigma_e = 6$ to $p = 1.3$ for $\sigma_e = 1600$. The break energy is roughly a few times σ_e . In general, these results are aligned with 2D simulations and 3D simulations without initial turbulence (Sironi & Spitkovsky 2014; Guo et al. 2014, 2015; Werner et al. 2016). While the reconnection X-points are strongly modified by the injected fluctuations and self-generated fluctuation due to secondary tearing and kink instabilities, the acceleration of high-energy particles is robust and not strongly dependent on the injected turbulence (see more discussion below). This suggests that X-point acceleration is not essential for particle acceleration in forming power-law distributions, as concluded by Guo et al. (2019) and 3D nonrelativistic studies (Dahlin et al. 2017; Li et al. 2019b; Zhang et al. 2021). Nevertheless, these results suggest that relativistic magnetic reconnection is a robust mechanism for producing nonthermal particle acceleration even in the presence of large-amplitude turbulence.

3.2.2. Acceleration Mechanism

We now discuss the acceleration of energetic particles to high energy during RTMR. Figure 12 shows several sample trajectories presented as particle energy $(\gamma - 1)$ versus x . These particles are representative ones that are accelerated to very

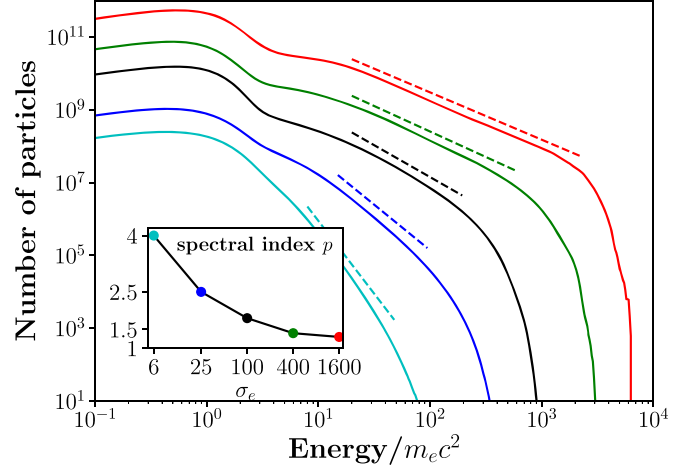


Figure 11. Particle energy spectra at the end of the simulations for different 3D runs with injected turbulence amplitude $\delta B^2/B_0^2 = 0.1$ and different $\sigma_e = 6$ –1600 (shifted vertically to show the difference). The inset shows spectral index for each energy spectrum.

high energy with γ reaching several hundred. The color of the curves represents the flow velocity at the particle location in the x -direction V_x . These particle trajectories clearly show Fermi bounces, during which particles gain a significant amount of energy when they have head-on “collisions” with the reconnection-generated flows (due to either outflow in the exhaust region or flux rope motions). We have examined hundreds of trajectories and find that this Fermi acceleration process is the main acceleration mechanism for particles accelerated to high energy. While earlier studies have included analyses of particle acceleration are still based on 2D simulations (e.g., Guo et al. 2014, 2015, 2019). Therefore, it is important to confirm that Fermi acceleration is still the dominant acceleration process in 3D RTMR simulations.

While analyzing particle trajectories is important for identifying basic acceleration patterns, this has generated significant controversy and confusion in the past, as the presented trajectories are limited to several subjectively hand-selected particles. Therefore, it is important to study the acceleration

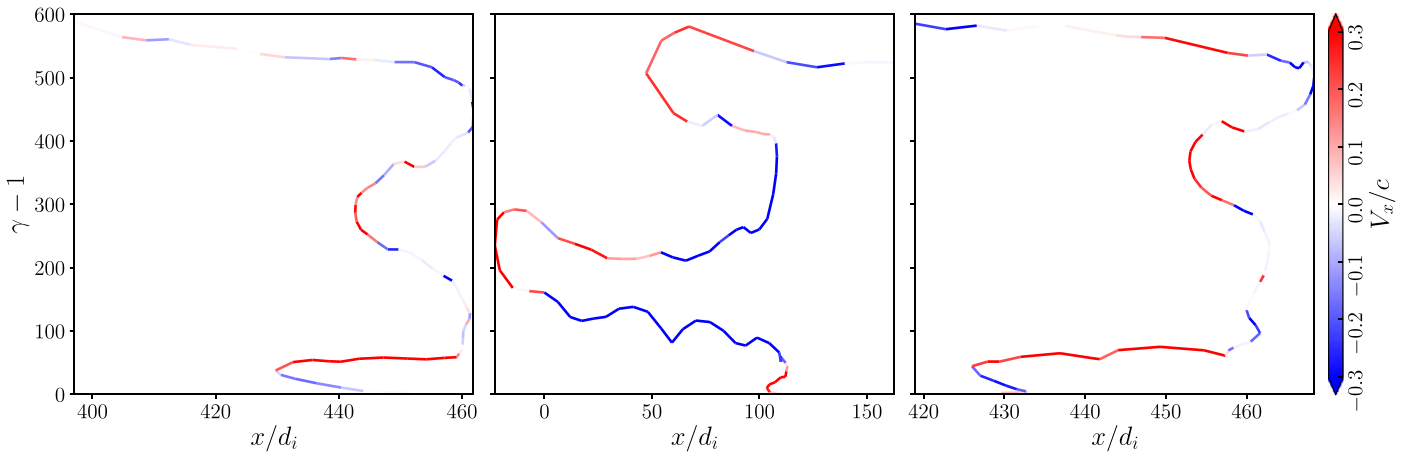


Figure 12. Several particle trajectories showing energy versus x -position. The color on the curve represents fluid velocity in the x -direction V_x . These clearly show that Fermi bounces still exist in 3D turbulent reconnection.

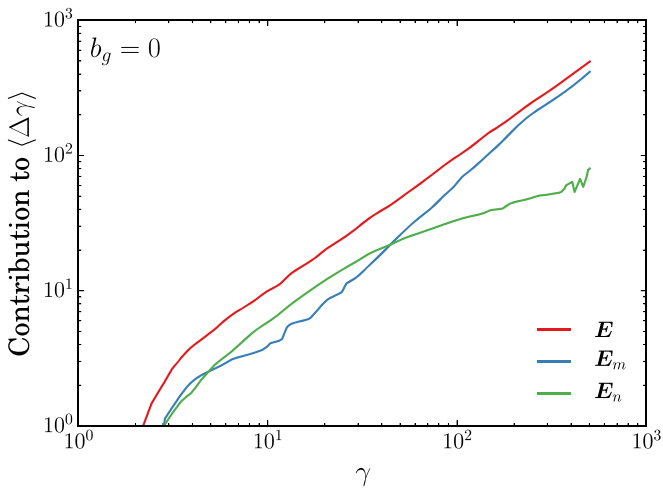


Figure 13. The averaged contribution of the motional electric field $\mathbf{E}_m = -\mathbf{V} \times \mathbf{B}/c$ vs. that of the nonideal electric field $\mathbf{E}_n = \mathbf{E} - \mathbf{E}_m$ to the total energy gain per particle in the standard run.

mechanisms statistically and consider all possibilities without bias. To show the dominant acceleration mechanism in a statistical way, we have performed another analysis using all 100 million tracer particles to calculate the energy gain in the motional electric field $\mathbf{E}_m = -\mathbf{V} \times \mathbf{B}/c$ (supporting Fermi acceleration) and nonideal electric field $\mathbf{E}_n = \mathbf{E} - \mathbf{E}_m$ (including X-point acceleration) (Guo et al. 2019). Figure 13 shows the contributions of \mathbf{E}_m and \mathbf{E}_n to the averaged total energy gain as a function of particle energy at the end of the simulation. The figure shows that Fermi-like acceleration, which is supported by motional electric field, dominates at high energy. This conclusion is similar to analysis made in 2D simulations (Guo et al. 2014, 2015, 2019), indicating that this acceleration process is not strongly modified by 3D effects. It is worth noting that the differences between particle acceleration in 2D and 3D relativistic reconnection appear to be smaller than their counterparts in the nonrelativistic regime (Dahlin et al. 2017; Li et al. 2019b; Zhang et al. 2021).

3D RTMR disfavors X-point acceleration, because this process relies on a channel along the nonideal electric field (y -direction in our simulation) with length $L_n > \Delta\gamma m_e c^2 / (qE_n)$, where $\Delta\gamma m_e c^2$ is the amount of energy gain and $E_n \sim 0.1B_0$ (see Liu et al. 2017, and discussion in Section 3.3). For $\Delta\gamma = 100$ in

the case with $\sigma_e = 100$, L_n has to be at least $100d_e$. This can hardly be satisfied because the kinked flux ropes perturb X-lines so an X-line does not form a potential channel in the y -direction, as we have shown in Figure 9. In addition, 3D simulations have shown that the 3D structure of the parallel electric field is patchy (Karimabadi et al. 2013), indicating that it is difficult for it to accelerate particles coherently, except at the beginning of the simulation. Although Fermi acceleration also relies on E_y , the motional electric field is usually 5–10 times larger than the nonideal electric field (Guo et al. 2019), and thus can accelerate particles over a much shorter distance. This is why we still observe clear Fermi bounces in RTMR simulations. The fact that the results of particle acceleration do not strongly depend on 3D effects favors Fermi acceleration and disfavors X-point acceleration as the main mechanism responsible for producing nonthermal particles in the reconnection region.

3.3. Reconnection Rate

The reconnection rate indicates the timescales for magnetic reconnection to dissipate magnetic field and the magnitude of electric field that accelerates particles to high energy. Figure 14 shows the time-dependent reconnection rate normalized using the initial asymptotic magnetic field $R = E_{\text{rec}}/B_0$ in run 3D-1. This is measured using a technique that determines the separatrices by finding the plasma mixing boundary of particles in an upper box ($z > 0$) and a lower box ($z < 0$), described by Daughton et al. (2014). Because of the initial driving, the current layer quickly becomes unstable, as shown in Figure 2, and particles from the upper and lower half-boxes can efficiently mix with each other by following the turbulent magnetic field lines (see more discussions in Section 3.6). As a result, reconnection occurs quickly and starts to convert energy violently, and the reconnection rate starts to be fast, $R \sim 0.1$. The rate peaks around $R = 0.15$ and gradually settles to about 0.07. Figure 15 shows the peak reconnection rate for different σ_e . The peak rate increases with σ_e and may saturate around $R \sim 0.2$. This result is in general consistent with results from earlier 2D and 3D reconnection simulations in the relativistic regime (Guo et al. 2015; Liu et al. 2015, 2017) and simulations in the nonrelativistic regime (Liu et al. 2017; Daughton et al. 2014), suggesting that the injected and self-generated turbulence cannot enhance the reconnection rate in kinetic simulations. This may contradict the predictions from turbulent

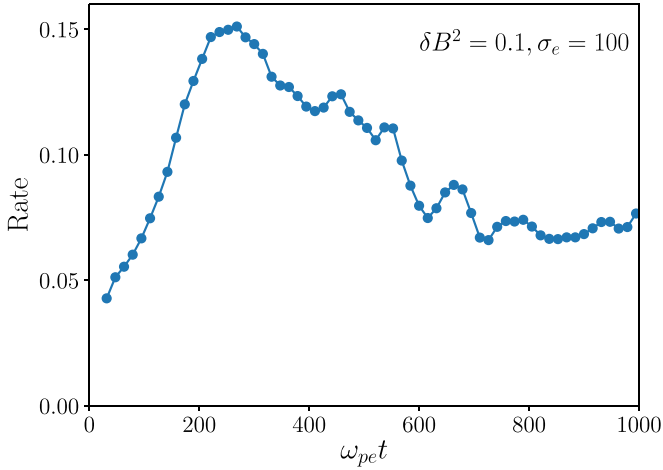


Figure 14. Time evolution of the reconnection rate $R = E_{\text{rec}}/B_0$ in run 3D-1, where E_{rec} is the reconnection electric field. The peak rate is about 0.15, consistent with 2D simulations despite the existence of turbulence.

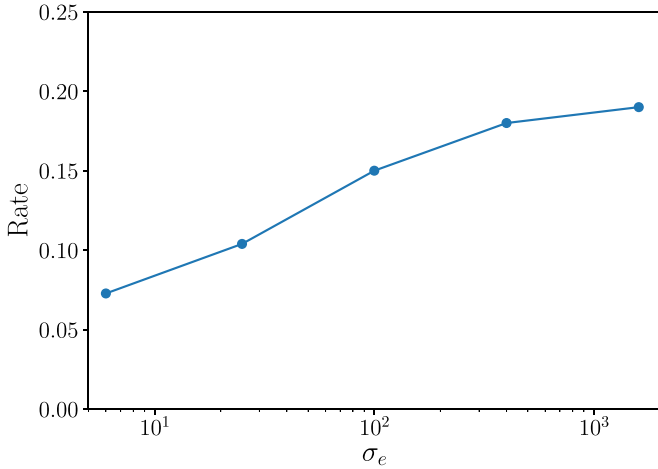


Figure 15. The peak reconnection rate as a function of σ_e . The peak rate increases with σ_e .

reconnection models (Lazarian & Vishniac 1999) but is understandable because the reconnection rate in kinetic simulations without driving already approaches the theoretical upper limit (Liu et al. 2017). The consistent result across different simulations suggests a universal value for magnetic reconnection rate in the magnetically dominated regime, at least for reconnection starting from a long current sheet with thickness of tens of skin depths.

3.4. Dependence on Turbulence Amplitude

In existing theories and MHD simulations of turbulent reconnection, the turbulence amplitude strongly influences the reconnection rate and particle acceleration (Lazarian & Vishniac 1999; Kowal et al. 2009). Here we use a series of kinetic simulations with initial driving to examine the role of initial turbulence amplitude on reconnection rate. With the same set of runs, we also study how initial turbulence affects particle acceleration.

Figure 16 compares reconnection rate as a function of time for different initial perturbation amplitudes $\delta B^2/B_0^2 = 0, 0.1, 0.2,$ and 0.4 . We note that even for the case with $\delta B^2 = 0$, there are still substantial self-generated fluctuations because of secondary tearing and kink instability, similar to earlier studies (Guo et al.

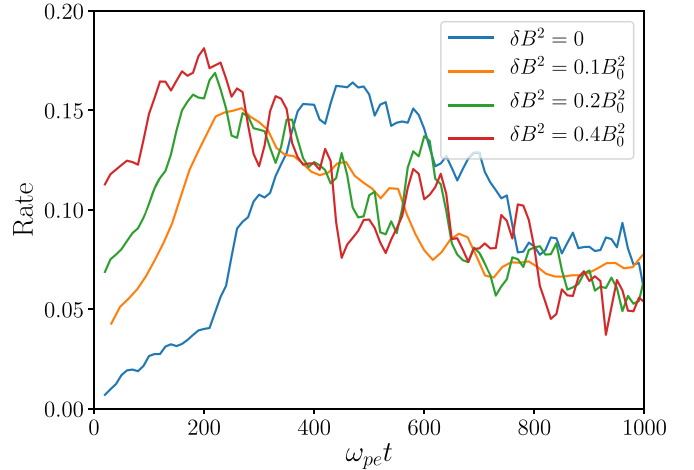


Figure 16. The reconnection rate for the runs with different turbulence amplitudes. The injected fluctuation leads to a shorter onset time where reconnection becomes fast, $R \sim 0.1$. The peak reconnection rate does not depend strongly on the turbulence amplitude.

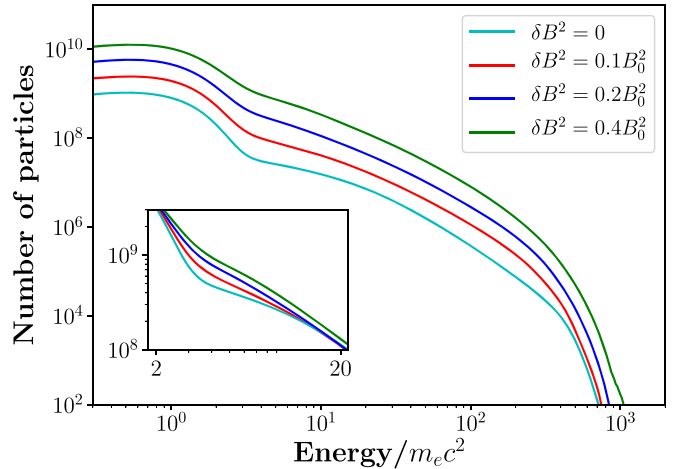


Figure 17. Energy spectra for different turbulence amplitudes (slightly shifted up or down against each other). The inset compares their absolute flux in the range $2 < \gamma - 1 < 20$. The effect of turbulence accelerates more low-energy particles but has not much effect on the high-energy power-law spectrum.

2014, 2015). Figure 16 shows that the peak reconnection rate does not depend strongly on the turbulence level. This suggests that for the regime we explore, the peak reconnection rate may still be determined by kinetic physics, as indicated in Figure 3. This result is also in contrast with recent MHD simulations at high Lundquist number (Yang et al. 2020), which show that the reconnection rate is around $R \sim 0.01$ without turbulence injection, and that injected turbulence does enhance the reconnection rate to $R \sim 0.1$. Although the presence of initial turbulence does not change the peak reconnection rate, simulations with higher initial driving onset achieve peak reconnection rate faster. This would indicate the turbulence can accelerate the “triggering” process even if the rate does not change much.

Figure 17 shows particle energy spectra for runs with different initial turbulence amplitudes. Each of the spectra is slightly shifted up or down to show the difference. One would expect that the injected turbulence contributes to plasma heating and/or particle acceleration. We observe that the flux of the heated part of the distribution $\gamma \lesssim 20$ is increased for

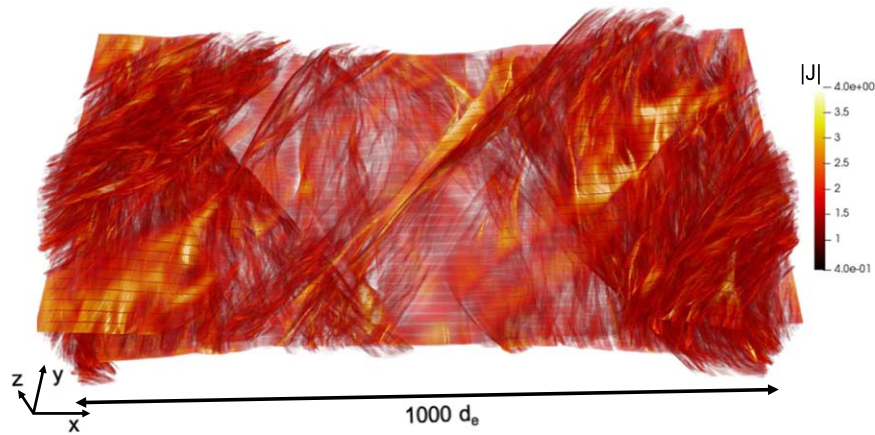


Figure 18. Structure of the reconnection layer for the case with guide field $b_g = 1$ shown using volume rendering of the current density. The reconnection is dominated by flux ropes from the oblique tearing instability.

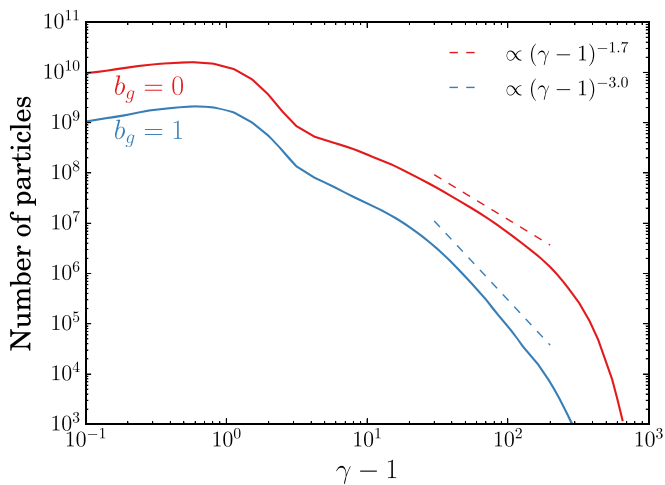


Figure 19. Particle energy spectra in the case with $b_g = 1$ (3D-6) compared to the case with $b_g = 0$ (3D-1). In both cases σ_e calculated based on the reconnecting magnetic field is 100. The acceleration of particles is less efficient in the presence of a strong guide field.

cases with higher turbulence injection (shown in the inset). The thermal core shifts to higher energies as the turbulence amplitude increases because the initial turbulence heats plasma. However, the high-energy spectra above $\gamma > 20$ are nearly identical in terms of flux, spectral index, and maximum energy. This result shows that the nonthermal particle acceleration is determined by the reconnection dynamics rather than the background turbulence.

3.5. Guide Field Dependence

We briefly discuss how a guide field will change reconnection dynamics and particle acceleration processes. Figure 18 shows the structure of the reconnection layer with $b_g = 1$, represented by a volume rendering of the current density. One can clearly see the generation of flux ropes oriented obliquely to the guide field direction due to the oblique tearing mode (Daughton et al. 2011; Liu et al. 2013). The interaction between flux ropes at different angles leads to a turbulent reconnection layer. The kink mode is suppressed by the guide field (Zenitani & Hoshino 2008). In Figure 19, we show the particle energy spectra in the case with $b_g = 1$ compared to the case with $b_g = 0$. We find that high-energy particle acceleration becomes

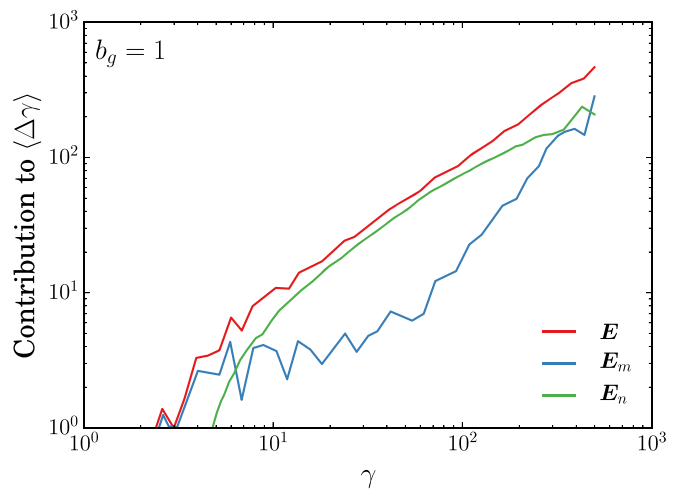


Figure 20. The averaged contribution of the motional electric field $E_m = -V \times B/c$ vs. that of the nonideal electric field E_n to the total energy gain per particle for the case with $b_g = 1$.

less efficient and the high-energy spectrum becomes softer, with a spectral index about $p = 3.0$.

To understand why the acceleration is less efficient, we perform statistical analysis of acceleration processes and show the results in Figure 20. We find that the nonideal acceleration dominates particle acceleration except at the highest energies, which is different from the run when $b_g = 0$ (Figure 13). At higher energy the contribution of Fermi acceleration does become comparable to that of the nonideal electric field acceleration. We would expect that the Fermi mechanism will dominate the acceleration processes in larger simulations where particles can be accelerated to higher energies. The relative contributions are similar to the finding in the nonrelativistic case (Dahlin et al. 2014; Li et al. 2018a). Li et al. (2018a, 2018b) have discussed the main controlling physics for this difference (see also le Roux et al. 2015). In the regime of weak guide field and low β (or high σ), the reconnection layer is highly compressible. This in fact facilitates particle acceleration through a Fermi-like process. When the guide field is stronger, however, the guide field component can prevent the collapse of the reconnection layer, reducing the compressibility and plasmoid formation (Liu et al. 2020), thus the Fermi process is suppressed and the relative contribution of the nonideal

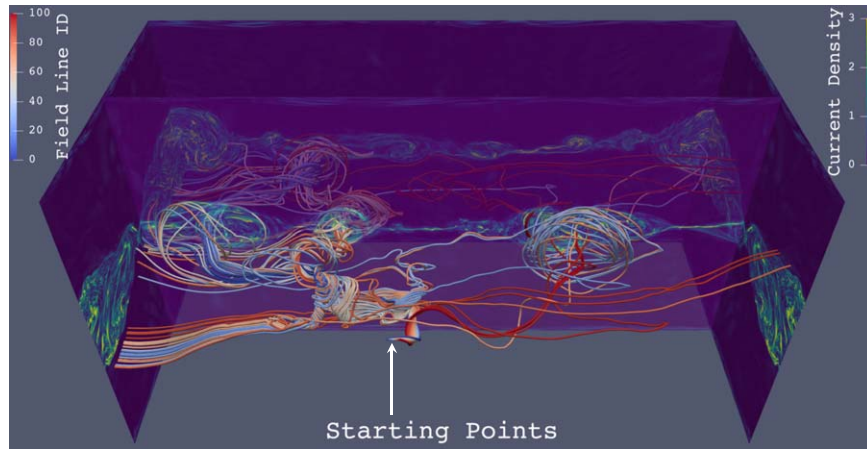


Figure 21. Chaotic magnetic field lines starting from 100 points that are uniformly distributed along a line segment with a length of $19d_e$ along $z = 0$. The greenish cuts show the current density. The field lines quickly diverge from each other and access the whole simulation domain. Some of the field lines form flux bundles and closely trace the flux ropes. The diverged field lines can also come close to each other again.

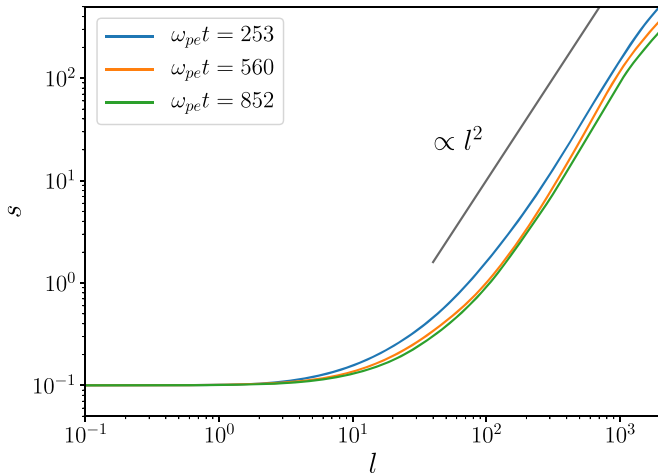


Figure 22. Field line diffusion based on the 3D kinetic reconnection simulation run 3D-1. The three curves in the plots are made using three snapshots at time steps corresponding to $\omega_{pe}t = 253$, 560, and 852, respectively. They represent at-peak, post-peak, and quasi-steady stages of reconnection, respectively. They all appear to follow a superdiffusive behavior with $s \propto l^2$.

electric field is more important. These results suggest that efficient particle acceleration in magnetic reconnection prefers a weak guide field with $b_g < 1$.

3.6. Superdiffusion of Magnetic Field Lines in the Reconnection Layer

In some reconnection models (e.g., Lazarian & Vishniac 1999), the concept of superdiffusion of magnetic field lines is essential for generating fast turbulent reconnection. Meanwhile, a range of instabilities and kinetic effects have been shown to lead to fast reconnection (Loureiro et al. 2007; Daughton et al. 2006, 2009; Drake et al. 2008; Liu et al. 2020). In our simulations, the reconnection rate stays around $R = 0.1$ while reconnection is in a turbulent state. It is therefore interesting to test some aspects of the superdiffusion concept in our 3D kinetic simulations with physical dimension $L_x/d_e = 1000$. Figure 21 shows some sample magnetic field lines in the reconnection layer in the standard run. There are 100 field lines that start uniformly in a line segment of length $19d_e$ along the x -direction at $z = 0$. The snapshot is at time $\omega_{pe}t = 560$. These field lines are integrated until they reach a

simulation boundary. Because of turbulence in the reconnection layer, field lines can quickly separate from each other and connect to different flux ropes in the simulation.

To quantify the magnetic field diffusion during reconnection, we adopt the following procedure in our simulations: using a magnetic field output at a particular time step, we trace two field lines by starting from a pair of positions that are closely spaced (the typical initial separation is $s_0 = 0.1d_e$). We calculate the separation between them s as a function of field line path length l . Pairs at different locations close to the center of the initial current sheet layer ($z = 0$) are chosen randomly. We have used 10^5 pairs to enhance the statistics. Figure 22 shows the results of field line separation as a function of field line length. At three different time steps $\omega_{pe}t = 253$ (peak reconnection rate), 560 (post-peak), and 852 (quasi-steady), $s(l)$ follows a relation close to l^2 instead of $l^{1/2}$ for diffusion until it starts to roll over at $l \sim 10^3 d_e$. Overall, we find that magnetic field lines indeed separate from each other at a rate much faster than the regular diffusion process. We have chosen two other initial heights ($z = 2\lambda$ and $z = 4\lambda$) for tracing field lines, and their behavior is quite similar. Furthermore, such analyses were done using snapshots at three different times capturing the at-peak and post-peak reconnection stages. This suggests that magnetic field lines exhibit superdiffusive behavior. The relatively narrow range of this exponent also suggests that the initially injected turbulence might have strongly regulated the diffusive behavior, though the turbulence produced by 3D kinetic reconnection could have impacted the diffusive dynamics. More detailed analyses are needed to determine whether the injected and self-generated turbulence could lead to different field line diffusion behavior and how they might interact with each other.

While magnetic field lines exhibit superdiffusive behavior throughout the reconnection process, the peak reconnection rate does not appreciably depend on the injected turbulence amplitude. The reason for this is not clear (Figure 16). One possibility is that the reconnection rate in kinetic reconnection is already close to its upper bound due to the force balance in the reconnection region (Liu et al. 2017), and the additional effect of turbulence cannot enhance the rate by any significant factor. This suggests that several different factors, rather than a single mechanism, can contribute to the measured reconnection

rate. More effort is needed to identify the main mechanism for fast turbulent reconnection.

4. Observational Implication

We now discuss the implication of the above results for understanding the role of RTMR in magnetically dominated astrophysical systems. It is generally believed that as relativistic jets from black holes or pulsar winds are launched, the flow is dominated by magnetic field with $\sigma \gg 1$. Relativistic magnetic reconnection is likely to be present in both relativistic jets and pulsar winds (Giannios & Uzdensky 2019; Coroniti 1990). The conversion of magnetic energy into particle kinetic energy leads to strong particle energization and high-energy radiation. While earlier 2D studies show that the reconnection layer is filled with fast moving plasmoids that can be approximated as 2D structures, our 3D simulations show a very different picture: RTMR develops in a fully 3D way with 3D instabilities and externally driven turbulence. These 3D features may have a strong impact on high-energy emissions in those systems. Our simulations call into question previous radiation models based on 2D relativistic reconnection (Sironi et al. 2016; Petropoulou et al. 2016; Zhang et al. 2018), which rely on the more ordered 2D plasmoid structures. Specifically, when 3D effects are considered, the averaged outflow speed becomes much slower; the plasmoid-like structures become quite dynamical and unstable, and cannot be approximated as a cylinder, ellipse, or sphere, as assumed by previous 2D reconnection models. Thus fully 3D radiation modeling is needed to capture the 3D features of RTMR. In the following, we discuss qualitatively the consequences of these 3D features of RTMR for observable signatures.

4.1. Nonthermal Spectrum

The overall RTMR nonthermal particle distributions and the resulting radiation spectra are similar to their 2D counterparts. Generally speaking, the observed high-energy emission from relativistic jets and pulsar winds requires the acceleration of a nonthermal power-law energy distribution of particles extending to very high Lorentz factors. The results presented in this paper further demonstrate that power-law energy spectra of particles are a generic outcome of magnetic reconnection in the magnetically dominated regime, even when the reconnection process occurs in a turbulent state. The spectral index depends on the magnetization σ_e and varies from a soft spectrum ($p = 4$ or softer) for small σ_e to a hard spectrum when σ_e is large. In the limit of large σ_e (strong acceleration), the hardest spectrum appears to have $p \sim 1$, which is harder than the value usually quoted for shock acceleration of $p \sim 2.2$ – 2.3 (Achterberg et al. 2001; Keshet & Waxman 2005; Yan et al. 2016). In addition, the presence of the guide field can appreciably weaken the acceleration rate, leading to smaller maximum particle energy and a softer power-law spectrum.

4.2. Acceleration Timescale and Variability

The current results for RTMR further demonstrate that magnetic reconnection is an efficient mechanism for quickly dissipating magnetic energy in highly magnetized plasmas. The strong radiative cooling and fast flaring activities observed in many high-energy astrophysical systems have suggested the importance of very efficient particle acceleration (Aharonian et al. 2007; Abdo et al. 2011), in favor of fast reconnection. Our simulations

suggest that external turbulence can be an effective mechanism for triggering magnetic reconnection, leading to a sudden energy release and efficient particle acceleration, consistent with observations. With the existence of turbulence, fast reconnection quickly kicks in and accelerates particles to high energy within a fraction of the light-crossing time. However, the strong turbulence and instabilities present in RTMR make the plasmoid-like structures very unstable. As a result, the previous models relying on fast moving plasmoids to explain fast variability in relativistic jets may be oversimplified.

4.3. Polarization

The strong 3D turbulence and instabilities in RTMR predict very different polarization signatures from their 2D counterparts. Due to the externally applied and/or self-generated turbulence in the reconnection layer, we expect a relatively low polarization degree during reconnection. This can explain the typically observed optical polarization degree of blazars at $\sim 10\%$ level. And the Imaging X-ray Polarimetry Explorer may also expect relatively low X-ray polarization in the Crab pulsar wind nebula (Weisskopf 2018). Furthermore, previous 2D reconnection models often simply assume that the plasmoids appear as straight flux ropes or plasma spheres in 3D (Sironi et al. 2016; Petropoulou et al. 2016; Zhang et al. 2018). As shown in our simulations, the flux ropes are curved and twisted, and can easily get disrupted. Due to the light-crossing delay, the light curves, especially at viewing angle other than face-on, can appear very different from the 2D simulation results, which demands further studies. Nonetheless, we observe that, similar to the 2D plasmoids, the 3D flux ropes can also merge into each other. In addition, these twisted structures can also change in time. Both features can potentially lead to considerable rotations in polarization angle at any viewing angle. Obviously, the swings in polarization angle are accompanied by blazar flares, due to the strong particle acceleration. Very interestingly, observations have shown that optical angle swings in blazars are always simultaneous with Fermi γ -ray flares (Blinov et al. 2018). In addition, the polarization degree generally drops during the changes in angle. These features are consistent with the evolution of reconnection shown in our simulations, and can be evidence for reconnection in blazar jets.

5. Conclusion

Thanks to the development of petascale computing and upcoming exascale computers, large-scale particle-in-cell plasma kinetic simulations will allow us to explore 3D plasma dynamics in various processes in an unprecedented way. In this work, we have explored the roles of external turbulent magnetic field in plasma dynamics and particle acceleration in relativistic turbulent magnetic reconnection. We find that during RTMR the current layer breaks up and the reconnection region quickly evolves into a turbulent layer filled with many coherent structures such as flux ropes and current sheets. The plasma dynamics in RTMR is quite different from its 2D counterpart in many aspects. The flux ropes evolve rapidly after their generation, and can be completely disrupted by the secondary kink instability. However, nonthermal particle acceleration and the timescale for energy release can be very fast and robust, even in the presence of turbulence. We observe clear power-law energy spectra in the magnetically dominated RTMR regime (from $p \sim 4$ when $\sigma_e = 6$ to $p \sim 1.3$ when

$\sigma_e = 1600$). The main acceleration mechanism for the low-guide-field limit is a Fermi-like acceleration process supported by the motional electric field induced by plasma flows in the reconnection layer, whereas the nonideal electric field acceleration plays a subdominant role (Litvinenko 1996; Sironi & Spitkovsky 2014). When a significant guide field exists, the kink instability is suppressed and oblique tearing instability becomes the dominant mode that leads to 3D turbulent reconnection (Daughton et al. 2011). In this case the nonideal electric field can dominate low-energy acceleration, but Fermi acceleration can quickly catch up because its scaling is proportional to energy, suggesting that Fermi acceleration is more important in high-energy acceleration. In addition, we observe that the averaged plasma flow speed in the reconnection layer can be significantly reduced due to the effect of turbulence. These findings have strong implications for high-energy astrophysical systems such as pulsars, jets from black holes, and gamma-ray bursts.

We have also investigated the superdiffusive behavior of magnetic field lines in RTMR. Our analysis suggests that superdiffusion is likely a generic feature of field lines in RTMR. However, for the simulation parameters we explored so far, the reconnection rate is still determined by kinetic physics, as the 3D reconnection rate is similar to its 2D counterpart.

We are grateful for support from DOE through the LDRD program at LANL and DoE/OFES support to LANL, and NASA ATP program through grant NNH17AE681. F.G. and W.D. acknowledge support in part from NASA Grant 80NSSC20K0627. The work by X.L. and Y.L. is funded by the National Science Foundation grant PHY-1902867 through the NSF/DOE Partnership in Basic Plasma Science and Engineering and NASA MMS 80NSSC18K0289. The research by P.K. was also supported by the LANL through its Center for Space and Earth Science (CES). CES is funded by LANL's Laboratory Directed Research and Development (LDRD) program under project number 20180475DR. Simulations and analysis were performed on LANL Trinity machine during its open science period. Additional simulations and analysis were performed at National Energy Research Scientific Computing Center (NERSC) and with LANL institutional computing.

ORCID iDs

Fan Guo  <https://orcid.org/0000-0003-4315-3755>
 Xiaocan Li  <https://orcid.org/0000-0001-5278-8029>
 William Daughton  <https://orcid.org/0000-0003-1051-7559>
 Hui Li  <https://orcid.org/0000-0003-3556-6568>
 Patrick Kilian  <https://orcid.org/0000-0002-8906-7783>
 Yi-Hsin Liu  <https://orcid.org/0000-0001-5880-2645>
 Qile Zhang  <https://orcid.org/0000-0002-9504-641X>
 Haocheng Zhang  <https://orcid.org/0000-0001-9826-1759>

References

- Abdo, A. A., Ackermann, M., Ajello, M., et al. 2011, *Sci*, **331**, 739
 Achterberg, A., Gallant, Y. A., Kirk, J. G., & Guthmann, A. W. 2001, *MNRAS*, **328**, 393
 Aharonian, F., Akhperjanian, A. G., Bazer-Bachi, A. R., et al. 2007, *ApJL*, **664**, L71
 Arons, J. 2012, *SSRv*, **173**, 341
 Beresnyak, A. 2017, *ApJ*, **834**, 47
 Biskamp, D. 2000, *Magnetic Reconnection in Plasmas*, Vol. 3 (Berlin: Springer)
 Blackman, E. G., & Field, G. B. 1994, *PhRvL*, **72**, 494
 Blinov, D., Pavlidou, V., Papadakis, I., et al. 2018, *MNRAS*, **474**, 1296
 Bowers, K., & Li, H. 2007, *PhRvL*, **98**, 035002
 Bowers, K. J., Albright, B. J., Yin, L., Bergen, B., & Kwan, T. J. T. 2008, *PhPI*, **15**, 055703
 Cho, J., & Vishniac, E. T. 2000, *ApJ*, **539**, 273
 Comisso, L., & Asenjo, F. A. 2014, *PhRvL*, **113**, 045001
 Coroniti, F. V. 1990, *ApJ*, **349**, 538
 Dahlin, J. T., Drake, J. F., & Swisdak, M. 2014, *PhPI*, **21**, 092304
 Dahlin, J. T., Drake, J. F., & Swisdak, M. 2017, *PhPI*, **24**, 092110
 Daughton, W., & Karimabadi, H. 2007, *PhPI*, **14**, 072303
 Daughton, W., Nakamura, T. K. M., Karimabadi, H., Roytershteyn, V., & Loring, B. 2014, *PhPI*, **21**, 052307
 Daughton, W., Roytershteyn, V., Albright, B. J., et al. 2009, *PhRvL*, **103**, 065004
 Daughton, W., Roytershteyn, V., Karimabadi, H., et al. 2011, *NatPh*, **7**, 539
 Daughton, W., Scudder, J., & Karimabadi, H. 2006, *PhPI*, **13**, 072101
 de Gouveia dalPino, E. M., & Lazarian, A. 2005, *A&A*, **441**, 845
 Drake, J. F., Shay, M. A., & Swisdak, M. 2008, *PhPI*, **15**, 042306
 Drake, J. F., Swisdak, M., Che, H., & Shay, M. A. 2006, *Natur*, **443**, 553
 Giannios, D., & Uzdensky, D. A. 2019, *MNRAS*, **484**, 1378
 Giannios, D., Uzdensky, D. A., & Begelman, M. C. 2009, *MNRAS*, **395**, L29
 Goldreich, P., & Sridhar, S. 1995, *ApJ*, **438**, 763
 Goldreich, P., & Sridhar, S. 1997, *ApJ*, **485**, 680
 Guo, F., Li, H., Daughton, W., & Liu, Y.-H. 2014, *PhRvL*, **113**, 155005
 Guo, F., Li, X., Daughton, W., et al. 2019, *ApJL*, **879**, L23
 Guo, F., Li, X., Li, H., et al. 2016, *ApJL*, **818**, L9
 Guo, F., Liu, Y.-H., Daughton, W., & Li, H. 2015, *ApJ*, **806**, 167
 Guo, F., Liu, Y.-H., Li, X., et al. 2020, *PhPL*, **27**, 080501
 Hoshino, M., & Lyubarsky, Y. 2012, *SSRv*, **173**, 521
 Huang, Y.-M., & Bhattacharjee, A. 2016, *ApJ*, **818**, 20
 Karimabadi, H., Roytershteyn, V., Daughton, W., & Liu, Y.-H. 2013, *SSRv*, **178**, 307
 Keshet, U., & Waxman, E. 2005, *PhRvL*, **94**, 111102
 Kilian, P., Li, X., Guo, F., & Li, H. 2020, *ApJ*, **899**, 151
 Kirk, J. G., & Skjæraasen, O. 2003, *ApJ*, **591**, 366
 Kowal, G., Falceta-Gonçalves, D. A., Lazarian, A., & Vishniac, E. T. 2017, *ApJ*, **838**, 91
 Kowal, G., Falceta-Gonçalves, D. A., Lazarian, A., & Vishniac, E. T. 2020, *ApJ*, **892**, 50
 Kowal, G., Lazarian, A., Vishniac, E. T., & Otmianowska-Mazur, K. 2009, *ApJ*, **700**, 63
 Lazarian, A., & Vishniac, E. T. 1999, *ApJ*, **517**, 700
 le Roux, J. A., Zank, G. P., Webb, G. M., & Khabarova, O. 2015, *ApJ*, **801**, 112
 Leake, J. E., Daldorff, L. K. S., & Klimchuk, J. A. 2020, *ApJ*, **891**, 62
 Li, X., Guo, F., & Li, H. 2019a, *ApJ*, **879**, 5
 Li, X., Guo, F., Li, H., & Birn, J. 2018a, *ApJ*, **855**, 80
 Li, X., Guo, F., Li, H., & Li, G. 2017, *ApJ*, **843**, 21
 Li, X., Guo, F., Li, H., & Li, S. 2018b, *ApJ*, **866**, 4
 Li, X., Guo, F., Li, H., Stanier, A., & Kilian, P. 2019b, *ApJ*, **884**, 118
 Litvinenko, Y. E. 1996, *ApJ*, **462**, 997
 Liu, Y.-H., Daughton, W., Karimabadi, H., Li, H., & Roytershteyn, V. 2013, *PhRvL*, **110**, 265004
 Liu, Y.-H., Guo, F., Daughton, W., Li, H., & Hesse, M. 2015, *PhRvL*, **114**, 095002
 Liu, Y.-H., Hesse, M., Guo, F., et al. 2017, *PhRvL*, **118**, 085101
 Liu, Y.-H., Lin, S.-C., Hesse, M., et al. 2020, *ApJL*, **892**, L13
 Loureiro, N. F., & Boldyrev, S. 2018, *ApJL*, **866**, L14
 Loureiro, N. F., Schekochihin, A. A., & Cowley, S. C. 2007, *PhPI*, **14**, 100703
 Loureiro, N. F., Uzdensky, D. A., Schekochihin, A. A., Cowley, S. C., & Yousef, T. A. 2009, *MNRAS*, **399**, L146
 Lyubarsky, Y., & Kirk, J. G. 2001, *ApJ*, **547**, 437
 Lyubarsky, Y. E. 2005, *MNRAS*, **358**, 113
 Lyutikov, M. 2003, *MNRAS*, **346**, 540
 Matthaeus, W. H., & Lamkin, S. L. 1985, *PhFI*, **28**, 303
 Matthaeus, W. H., & Lamkin, S. L. 1986, *PhFI*, **29**, 2513
 McKinney, J. C., & Uzdensky, D. A. 2012, *MNRAS*, **419**, 573
 Nathanail, A., Fromm, C. M., Porth, O., et al. 2020, *MNRAS*, **495**, 1549
 Petropoulou, M., Giannios, D., & Sironi, L. 2016, *MNRAS*, **462**, 3325
 Priest, E., & Forbes, T. 2007, *Magnetic Reconnection* (Cambridge: Cambridge Univ. Press)
 Sironi, L., Giannios, D., & Petropoulou, M. 2016, *MNRAS*, **462**, 48
 Sironi, L., & Spitkovsky, A. 2014, *ApJL*, **783**, L21
 Weisskopf, M. 2018, *Galax*, **6**, 33
 Werner, G. R., & Uzdensky, D. A. 2017, *ApJL*, **843**, L27

- Werner, G. R., Uzdensky, D. A., Cerutti, B., Nalewajko, K., & Begelman, M. C. 2016, [ApJL](#), **816**, L8
- Yan, D., He, J., Liao, J., Zhang, L., & Zhang, S.-N. 2016, [MNRAS](#), **456**, 2173
- Yan, D., & Zhang, L. 2015, [MNRAS](#), **447**, 2810
- Yang, L., Li, H., Guo, F., et al. 2020, [ApJL](#), **901**, L22
- Zenitani, S., & Hoshino, M. 2008, [ApJ](#), **677**, 530
- Zhang, B., & Yan, H. 2011, [ApJ](#), **726**, 90
- Zhang, H., Chen, X., Böttcher, M., Guo, F., & Li, H. 2015, [ApJ](#), **804**, 58
- Zhang, H., & Giannios, D. 2021, [MNRAS](#), **502**, 1145
- Zhang, H., Li, H., Guo, F., & Taylor, G. 2017, [ApJ](#), **835**, 125
- Zhang, H., Li, X., Giannios, D., et al. 2020, [ApJ](#), **901**, 149
- Zhang, H., Li, X., Guo, F., & Giannios, D. 2018, [ApJL](#), **862**, L25
- Zhang, Q., Guo, F., Daughton, W., Li, X., & Li, H. 2021, [arXiv:2105.04521](#)
- Zhou, M., Loureiro, N. F., & Uzdensky, D. A. 2020, [JPIPh](#), **86**, 535860401